Article

An Ultra-Broadband Polarization Beam Splitter Based on the Digital Meta-Structure at the 2 μm Waveband

Jiefeng Xu [1], Yingjie Liu [1], Xiaoyuan Guo [1], Jiangbing Du [2] and Ke Xu [1,*]

[1] Department of Electronic and Information Engineering, Harbin Institute of Technology, Shenzhen 518055, China; 21s052006@stu.hit.edu.cn (J.X.); 18b952051@stu.hit.edu.cn (Y.L.); 20s052007@stu.hit.edu.cn (X.G.)

[2] State Key Laboratory of Advanced Optical Communication Systems and Networks, Department of Electronic Engineering, Shanghai Jiao Tong University, Shanghai 200240, China; dujiangbing@sjtu.edu.cn

[*] Correspondence: kxu@hit.edu.cn

Abstract: The 2 μm waveband is considered to have great potential in optical communications. Driven by the demands on high-performance functional devices in this spectral band, various integrated photonic components have been demonstrated. In this work, an analog and digital topology optimization method is proposed to design an ultra-broadband polarization beam splitter at the 2 μm waveband. Within an optical bandwidth of 213 nm, the excess losses of TE and TM modes are <0.53 dB and 0.3 dB, respectively. The corresponding polarization extinction ratios are >16.5 dB and 18.1 dB. The device has a very compact footprint of only 2.52 μm × 5.4 μm. According to our best knowledge, this is a benchmark demonstration of an ultra-broadband and ultra-compact polarization beam splitter enabled by the proposed optimization method.

Keywords: inverse design; silicon photonics; polarization beam splitter

1. Introduction

Recently, the 2 μm waveband has shown great potential for optical communication applications. Several transmission experiments have been demonstrated for high-speed data transmission via optical fibers designed for 2 μm wavebands [1–4]. The communication window shifts to this waveband due to the ultra-low loss of optical fibers, the maturity of the narrow linewidth lasers, thulium doped fiber amplifier with 30 THz gain bandwidth [5], high-speed photodiode [6], and modulator [7–9]. Driven by the increasing demand for integrated components with low cost and high performance in the new waveband, rapid progress has been made in various devices such as optical switches [10], mode converters [11], mode multiplexers [12], grating couplers [13], power splitters [14], etc. These devices are realized by silicon photonics which offer the advantages of large fabrication volume and potential low cost.

However, the widely used silicon waveguide geometry introduces a strong birefringence, which exhibits a huge effective index difference between TE and TM modes. To overcome the birefringence issue on silicon, the polarization diversity circuit is often used where a polarization beam splitter (PBS) is one of the key devices to divide and combine optical waves with orthogonal polarizations. The on-chip silicon PBS has been widely studied and demonstrated at C-band using various techniques including multi-mode interference (MMI) couplers [15–17], Mach–Zehnder interferometers (MZIs) [18], 2D grating couplers [19–21], asymmetrical directional couplers (ADCs) [22–24], inversely designed meta-structure [25] and so forth. The MMI and MZI structures allow for high polarization extinction ratios (PER), which is normally >20 dB, but they normally occupy too much chip area. The polarization splitting grating couplers also have high polarization isolation with PER >20 dB, but the grating coupling loss is too high. PBS with an extremely small

footprint (2.4 μm × 2.4 μm) can be realized by utilizing complex meta-structures. However, the PER (<10 dB) and the optical bandwidth (32 nm) are quite limited.

In this paper, we propose an analog and digital topology optimization (ADTO) method and demonstrate it by an ultra-broadband PBS at a 2 μm band. The device has a PER of 16.5 dB and an optical bandwidth of 213 nm. The device has a small footprint of only 2.52 μm × 5.4 μm. Compared to that previously reported of the PBS at the 2 μm waveband [26], the footprint of our device is reduced by nearly 35 times. The performance advantages of the proposed PBS verify the effectiveness of the ADTO method, which has great potential for inverse design of high-performance on-chip photonic devices.

2. Device Design

The PBS is designed on a silicon-on-insulator (SOI) platform with 340 nm-thick top-silicon, 2 μm-thick buried dioxide and 500 nm-thick oxide top cladding. As shown in Figure 1a, the initial structure consists of three ports (Port-1, Port-2 and Port-3) and a Y-junction waveguide which is composed of 20 nm × 20 nm silicon pixels. The Y-junction, labeled by a blue dash line, is the optimization region. The widths of Port-1, Port-2 and Port-3 are all 600 nm, which satisfies single-mode condition at a 2 μm wavelength range. The gap distance between Port-2 and Port-3 is set to be 840 nm to avoid coupling. The design objective of the device can be described as: when TE (TM) mode is launched from Port-1, TE (TM) mode transmission efficiency will be maximized at the Port-2 (Port-3).
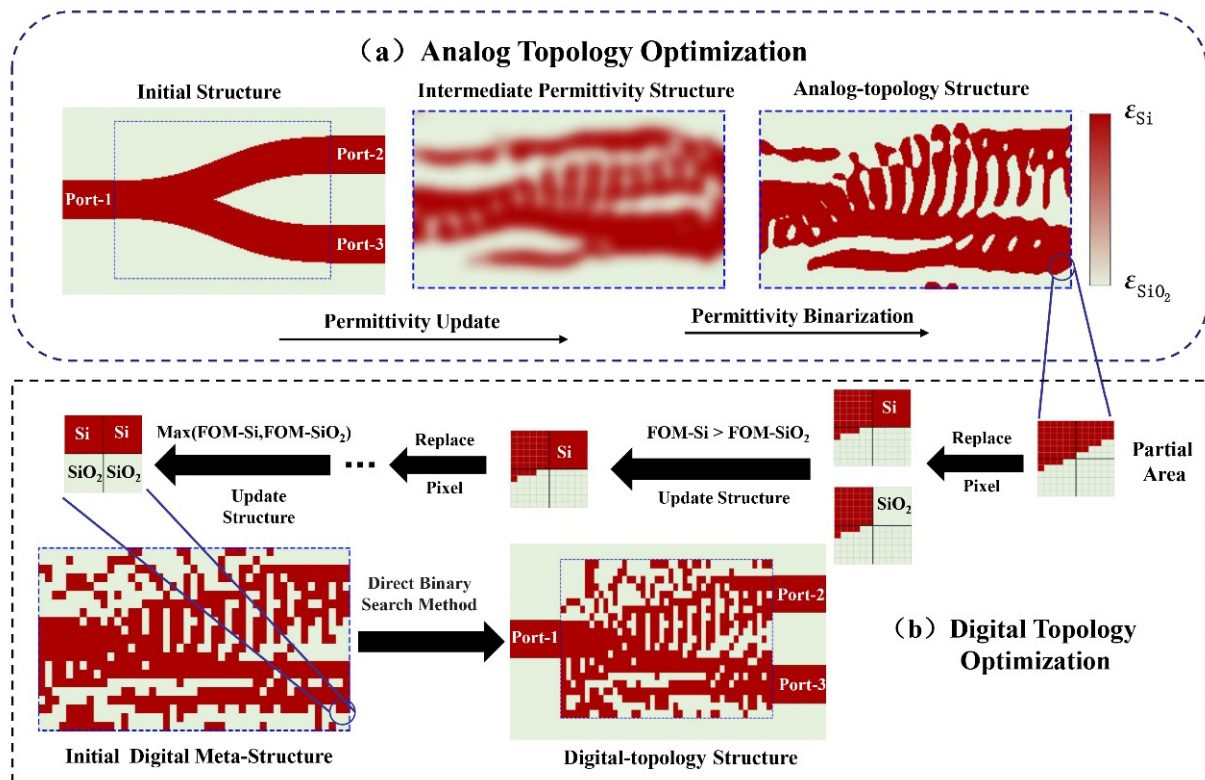

Figure 1. (**a**) and (**b**) are the processes of the ATO and DTO, respectively.

The transmission of the TE / TM mode can be obtained by the overlapping integration of the actual electric field and the mode electric field at the cross-section of Port-2/Port-3.

$$T_m = \frac{1}{8} \frac{\left| \int_S \left(E_{act} \times \overline{H_m} + \overline{E_m} \times H_{act} \right) dS \right|^2}{\int_S \mathrm{Re} \left(E_{act} \times \overline{H_m} \right) dS},$$

(1)

where S is the cross-section of the output waveguide. $E_{m/act}$ and $H_{m/act}$ represent the standard/actual electric and magnetic fields of the m-th mode at the cross-section S. The figure of merit (FOM) is defined as follows:

$$\text{FOM} = (\text{T}_{TE} + \text{T}_{TM})/2, \tag{2}$$

where T_{TE} (T_{TM}) is the average transmittance of TE (TM) mode at Port-2 (Port-3) from wavelengths 1900 nm–2100 nm. As depicted in Figure 1, the optimization process is divided into two stages: analog topology optimization (ATO) and digital topology optimization (DTO).

In the ATO stage, the design region with an area of 2.52 μm × 5.4 μm is divided into 270 × 126 pixels with dimensions of 20 nm × 20 nm. The permittivity of each pixel can be arbitrarily chosen within a range between ε_{Si} and ε_{SiO_2}. For the aforementioned FOM, the gradient information of all the pixels is obtained via the adjoint method [27]. Then, the material properties of all the pixels are iteratively optimized. Based on the Scipy package (an open-source package) [28] and gradient information, the L-BFGS-B method is used to update the pixel permittivity in each iteration. Then, an intermediate permittivity structure can be obtained, as indicated by the central structure in Figure 1a. Taking the fabrication feasibility into account, Heaviside filter equation is used to binarized the permittivities of all pixels [29,30]. Then, an analog-topology structure consisting of only silicon or oxide is obtained. It is worth noting that there are many nanoholes with too-small dimensions or extremely sharp corners in this structure, which is not compatible with the fabrication capability.

To solve this problem, we employ another DTO process. The design region is re-divided by a large-pixel matrix with a pixel size of 120 nm × 120 nm, which can be easily fabricated via a standard silicon photonic process. Figure 1b shows the analog-to-digital conversion of the structure. The material property of each large pixel will be either silicon or oxide, which is determined by examining the corresponding FOM defined as FOM-Si or FOM-SiO$_2$. By doing this, the analog-topology structure can be converted into an initial digital meta-structure, which can be potentially fabricated. Since this conversion sacrifices the device performance, the structure is further optimized via the direct binary search (DBS) method [31,32] to improve the FOM. Then, the digital-topology structure is obtained. In this paper, all electromagnetic simulations are performed by the three-dimensional finite difference time domain (3D FDTD) method [33].

3. Results and Discussions

Figure 2a shows the variation trend of FOM with the number of iterations. After 218 iterations, the analog-topology structure is obtained, and its FOM is 0.97. It can be seen that the analog-to-digital conversion degrades the device FOM from 0.97 to 0.86. The DTO process improves it from 0.86 to 0.93 via 220 iterations, and the digital-topology structure can be finally obtained. Based on an eight-core computer (Intel Core i7-9700K), the total optimization time is close to 98 h including both ATO and DTO processes. In Figure 2b, based on the same FOM expression, the DBS method is applied to a Y-shaped initial structure consisting of 120 nm × 120 nm pixels. After 700 iterations (254 h), the value of FOM stabilized at 0.85. Compared with the former, the ADTO method only takes 98 h to obtain a better result (FOM = 0.93). Of course, by trying different initial structures or adjusting the expression of the FOM, the DBS method may obtain better performance. However, this method increases the time cost. Furthermore, the DBS method optimizes the performance of devices by flipping pixel material properties one by one [31,32]. As the number of pixels increases, it is difficult for the DBS method to efficiently search the huge parameter space. The adjoint method is an efficient way to compute gradients, which is independent of the number of pixels [27]. In this paper, based on the adjoint method, the ADTO method only needs four 3D FDTD simulations to determine the optimization direction of all pixels in the ATO stage, which can effectively make up for the global search ability of the DBS method.
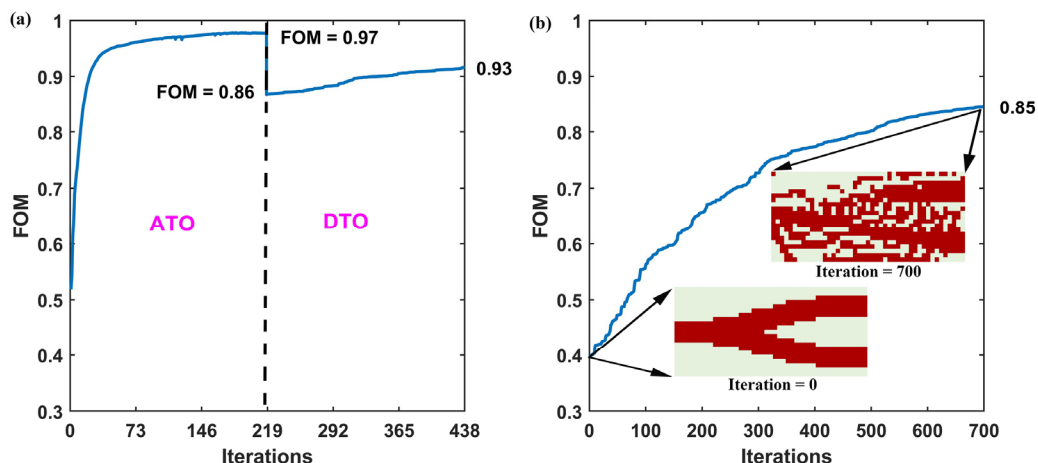
Figure 2. The optimization curves for (**a**) ADTO method and (**b**) DBS method.

The performance of the analog-topology structure is shown in Figure 3a. For TE and TM modes, the simulated excess losses (ELs) are <0.25 dB and the PERs are >20 dB over a wavelength range from 1879 nm–2094 nm. Although the performance of the device is excellent, the device cannot be fabricated. As shown in Figure 3b, in the wavelength range of 1860 nm–2136 nm, the ELs of the TE and TM modes are <1 dB and 0.72 dB for the initial digital meta-structure. The PERs are simulated to be >14.26 dB. Although the device performance of the initial digital structure is lower than that of the analog-topology structure, its fabrication reliability is guaranteed. The simulated optical field distributions of the PBS can be found in the insets of Figure 3.
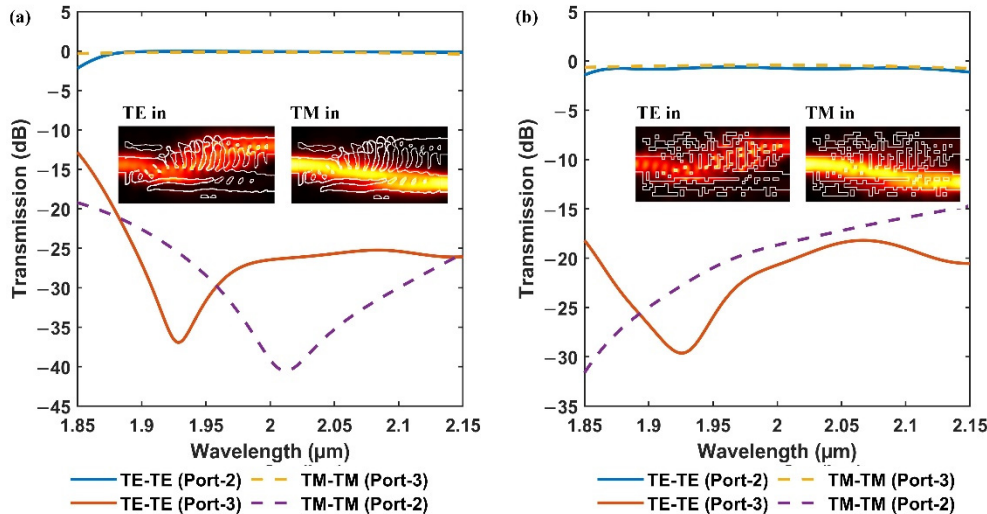

Figure 3. (**a**) and (**b**) are the transmission spectra of the analog-topology structure and the initial digital meta-structure, respectively.

For the digital-topology structure, the H_z/E_z field distributions of the TE/TM mode at different wavelengths (λ = 1900 nm, 2000 nm and 2100 nm) are shown in Figure 4. In Figure 4a–c, after the TE mode reaches Port-1, the propagation direction of the light will be adjusted by the digital-topology structure. Then, the TE mode is completely coupled into Port-2, and the light coupled into Port-3 is almost negligible. In contrast, the TM mode is obtained at Port-3 without being coupled into Port-2, as shown in Figure 4d–f. There is negligible mode conversion in the field distribution for both modes. The transmission spectra of the digital-topology structure are calculated in Figure 5. The EL is <0.53 (0.33) dB and the PER is >16.5 (18.1) dB from wavelength 1888 nm–2104 nm for the TE (TM) mode. At a central wavelength of 2 μm, ELs of TE and TM Modes are <0.36 dB and 0.18 dB,

respectively. Their PERs are both >20 dB. With a footprint of only 2.52 μm × 5.4 μm, the digital-topology structure achieves low ELs and high PERs for both TE and TM modes in a bandwidth of 213 nm. This result shows the reliability of the ADTO method.
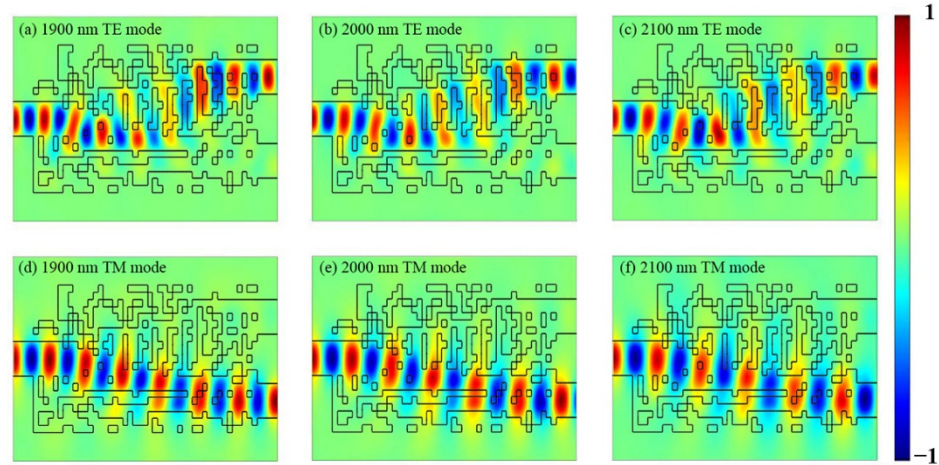

Figure 4. (**a**–**c**) and (**d**–**f**) are H_z field distributions of TE modes and E_z field distributions of the TM modes for the digital-topology structure, respectively.
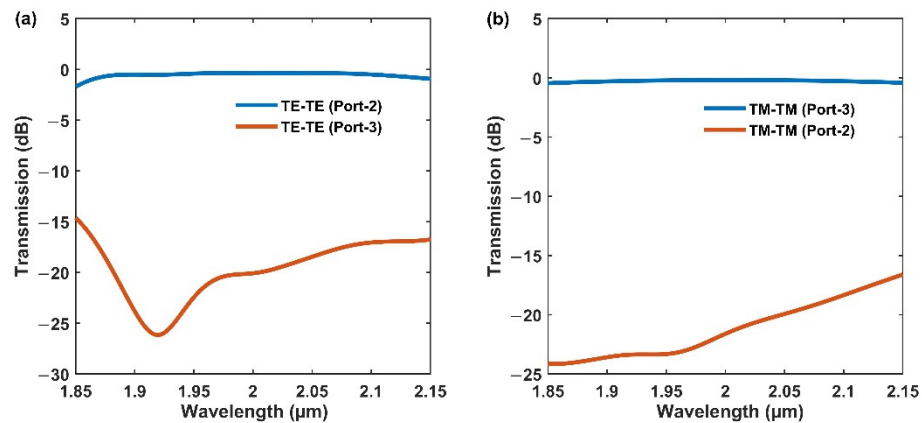

Figure 5. (**a**) and (**b**) are the transmission spectra of TE and TM modes for the digital-topology structure, respectively.

Then, we investigate the impact of device structure deviation induced by the random fabrication errors. In Figure 6a,b, the fabrication tolerance of the device is analyzed by varying the pixel size. When the pixel size variation is ±10 nm, the ELs of the TE and TM modes are <0.73 dB and 0.31 dB in a 194 nm bandwidth, respectively. Within the same bandwidth, PERs of TE and TM modes are >15 dB and 17.5 dB. In some cases, the oxide may not completely fill nanoholes, which causes small air gaps. In Figure 6c,d, the transmission curves for air gaps of different thicknesses (30 nm and 60 nm) are calculated. Since the air gap changes the refractive index profile of the device, the transmission curve is shifted close to 13 nm wavelength and the performance of the device is slightly degraded. From 1875 nm–2075 nm wavelengths, the ELs of TE and TM modes are <0.59 dB and <0.42 dB. Their PERs are both >19 dB. Therefore, the designed device has a good tolerance for fabrication errors. In addition, the ADTO method can also be extended to circular pixels, which can effectively reduce the influence of the lag effect [34].
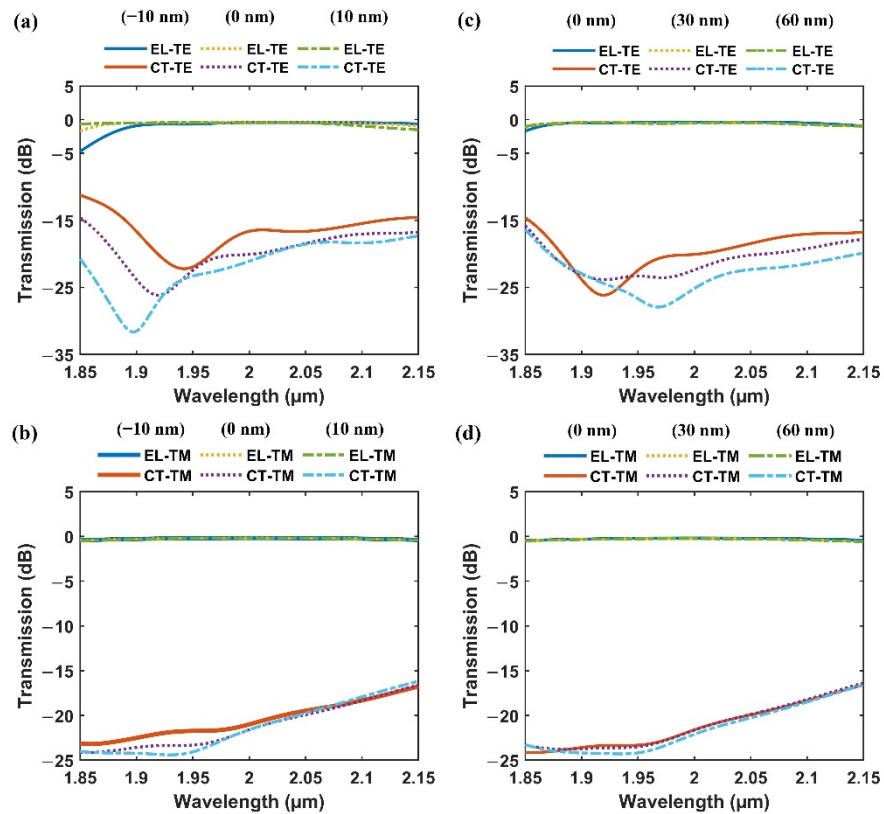
Figure 6. The transmission spectra with ±10 nm pixel size variations for (**a**) TE and (**b**) TM modes; the transmission spectra of (**c**) TE and (**d**) TM modes for different air gap thicknesses.

Some previous works have discussed how to improve the fabrication reliability of the analog-topology structure [35–37], which can effectively improve the structural integrity or constrain the minimum feature size of nanoholes. However, the minimum feature size is normally ≤100 nm in these works. Compared to the former, there are no irregular topological shapes in the design area for the ADTO method. In the optimized structure, each pixel nanohole can be easily fabricated via the standard silicon photonic process. What's more, for the ADTO method, the pixel size can be flexibly adjusted according to design requirements. Here, the ADTO method is additionally applied to design the PBS with a minimum feature size of 140 nm. At this time, the footprint of the device needs to be slightly modified to 2.52 μm × 5.46 μm. Figure 7a,b are the schematic diagram of the optimized device structure and the transmission spectrum, respectively. Obviously, due to the reduced freedom of device design, the performance degradation of PBS devices is inevitable, which can be solved by appropriately increasing the design space. However, from 1905 nm–2100 nm wavelengths, the ELs of TE mode and TM mode are still less than 0.76 dB and 0.47 dB, respectively.
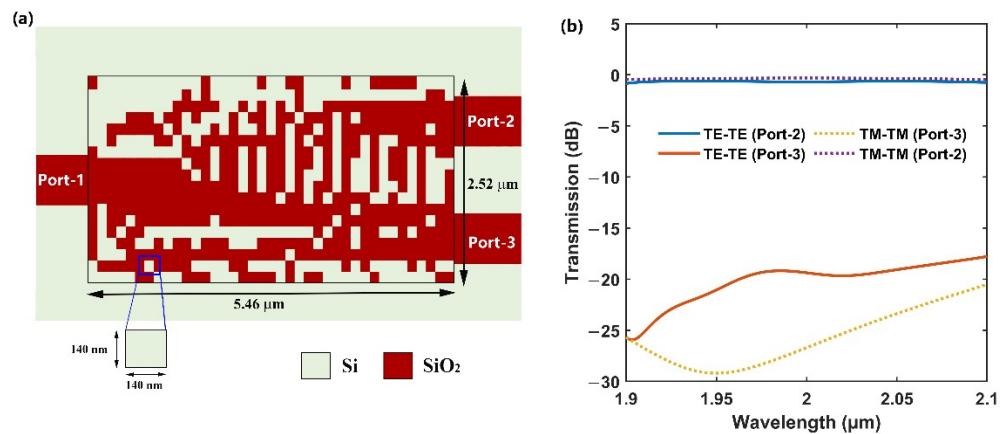
Figure 7. (**a**) The schematic diagram of the optimized PBS with a minimum feature size of 140 nm; (**b**) the corresponding transmission spectra of TE and TM modes.

To compare our work with other reported devices, Table 1 summarizes some typical ultra-broadband PBSs including 1.55 μm and 2 μm wavebands. Compared to previously reported PBSs of 2 μm wavebands [26], the footprint of the PBS is reduced by a factor of 35 in this paper. This result demonstrates the reliability of the proposed method. It is worth mentioning that the ADTO method can also be extended to the design of other on-chip optical devices such as power splitting devices, crossed waveguides, etc.

Table 1. The comparison of reported ultra-broadband PBSs.

Reference	Year	Footprint (μm^2)	TM Mode		TE Mode		BW * (nm)	Waveband
			EL (dB)	PER (dB)	EL (dB)	PER (dB)		
Xu et al. [38]	2019	12.25 × 1.9	<0.9	>20	<0.2	>20	215	1.55-μm
Herrero-Bermello et al. [39]	2020	92.4 × 4	<1.0	>20	<1.0	>20	130	1.55-μm
Li et al. [40]	2020	33.6 × 4.04	<0.3	>20	<0.3	>20	270	1.55-μm
Lin et al. [18]	2021	198.3 × 2.8	<0.5	>20	<0.5	>20	310	1.55-μm
Liu et al. [26]	2021	48 × 10	<0.5	>15	<0.02	>30	195	2-μm
Our Work		5.4 × 2.52	<0.33	>18.1	<0.53	>16.5	216	2-μm

* BW: bandwidth.

4. Conclusions

In summary, we propose the ADTO method for the inverse design of on-chip optics devices and demonstrate this method by an ultra-broadband PBS at the 2 μm waveband. The simulation results show the high performance of the device to divide TE and TM modes to corresponding output ports with low ELs and high PERs within a bandwidth of 213 nm. The on-chip area occupied by the device is much smaller than the PBSs reported in the literature, which demonstrates the effectiveness of this method. The proposed approach can also be extended to other on-chip optical devices.

Author Contributions: Conceptualization, Y.L. and J.X.; methodology, J.X. and X.G.; software, J.X.; validation, J.X.; formal analysis, J.X. and K.X.; investigation, J.X. and X.G.; resources, J.X. and K.X.; data analysis, J.X.; writing—original draft preparation, J.X. and K.X.; writing—review and editing, J.X. and K.X.; visualization, K.X.; supervision, K.X. and J.D.; project administration, K.X.; funding acquisition, K.X. All authors have read and agreed to the published version of the manuscript.

Institutional Review Board Statement: Not applicable.

Informed Consent Statement: Not applicable.

Data Availability Statement: The code can be obtained from the corresponding author upon reasonable request.

Conflicts of Interest: The authors declare no conflict of interest.

References

1. Xu, K.; Sun, L.; Xie, Y.; Song, Q.; Du, J.; He, Z. Transmission of IM/DD signals at 2-μm wavelength using PAM and CAP. *IEEE Photonics J.* **2016**, *8*, 1–7. [CrossRef]
2. Xu, K.; Wu, Q.; Xie, Y.; Tang, M.; Fu, S.; Liu, D. High speed single-wavelength modulation and transmission at 2μm under bandwidth-constrained condition. *Opt. Express* **2017**, *25*, 4528–4534. [CrossRef] [PubMed]
3. Li, Z.; Heidt, A.; Simakov, N.; Jung, Y.; Daniel, J.; Alam, S.U.; Richardson, D. Diode-pumped Wideband Thulium-doped Fiber Amplifiers for Optical Communications in the 1800–2050 nm Window. *Opt. Express* **2013**, *21*, 26450–26455. [CrossRef] [PubMed]
4. Shen, W.; Du, J.; Sun, L.; Wang, C.; Zhu, Y.; Xu, K.; Chen, B.; He, Z. Low-Latency and High-Speed Hollow-Core Fiber Optical Interconnection at 2-Micron Waveband. *J. Lightwave Technol.* **2020**, *38*, 3874–3882. [CrossRef]
5. Liu, Z.; Chen, Y.; Li, Z.; Kelly, B.; Phelan, R.; O'Carroll, J.; Bradley, T.; Wooler, J.P.; Wheeler, N.V.; Heidt, A.M.; et al. High-capacity directly modulated optical transmitter for 2-μm spectral region. *J. Lightwave Technol.* **2015**, *33*, 1373–1379. [CrossRef]
6. Dong, Y.; Wang, W.; Xu, S.; Lei, D.; Gong, X.; Guo, X.; Wang, H.; Lee, S.Y.; Loke, W.K.; Yoon, S.F.; et al. Two-micron-wavelength germanium-tin photodiodes with low dark current and gigahertz bandwidth. *Opt. Express* **2017**, *25*, 15818–15827. [CrossRef]
7. Van Camp, M.A.; Assefa, S.; Gill, D.M.; Barwicz, T.; Shank, S.M.; Rice, P.M.; Topuria, T.; Green, W.M. Demonstration of electrooptic modulation at 2165nm using a silicon Mach-Zehnder interferometer. *Opt. Express* **2012**, *20*, 28009–28016. [CrossRef]
8. Cao, W.; Hagan, D.; Thomson, D.J.; Nedeljkovic, M.; Littlejohns, C.G.; Knights, A.; Alam, S.U.; Wang, J.; Gardes, F.; Zhang, W.; et al. High-speed silicon modulators for the 2 μm wavelength band. *Optica* **2018**, *5*, 1055–1062. [CrossRef]
9. Wang, X.; Shen, W.; Li, W.; Liu, Y.; Yao, Y.; Du, J.; Song, Q.; Xu, K. High-speed silicon photonic Mach–Zehnder modulator at 2 μm. *Photonics Res.* **2021**, *9*, 535–540. [CrossRef]
10. Shen, L.; Huang, M.; Zheng, S.; Yang, L.; Peng, X.; Cao, X.; Li, S.; Wang, J. High-Performance Silicon 2 × 2 Thermo-Optic Switch for the 2-μm Wavelength Band. *IEEE Photonics J.* **2019**, *11*, 1–6.
11. Ruan, Z.; Shen, L.; Zheng, S.; Wang, A.; Long, Y.; Zhou, N.; Wang, J. Subwavelength grating slot (SWGS) waveguide at 2 μm for chip-scale data transmission. *Nanophotonics* **2018**, *7*, 865–871. [CrossRef]
12. Zheng, S.; Huang, M.; Cao, X.; Wang, L.; Ruan, Z.; Shen, L.; Wang, J. Silicon-based four-mode division multiplexing for chip-scale optical data transmission in the 2 μm waveband. *Photonics Res.* **2019**, *7*, 1030–1035. [CrossRef]
13. Li, J.; Liu, Y.; Meng, Y.; Xu, K.; Du, J.; Wang, F.; He, Z.; Song, Q. 2 μm Wavelength Grating Coupler, Bent Waveguide, and Tunable Microring on Silicon Photonic MPW. *IEEE Photonics Technol. Lett.* **2018**, *30*, 471–474. [CrossRef]
14. Xie, H.; Liu, Y.; Sun, W.; Wang, Y.; Xu, K.; Du, J.; He, Z.; Song, Q. Inversely designed 1 × 4 power splitter with arbitrary ratios at 2-μm spectral band. *IEEE Photonics J.* **2018**, *10*, 1–6. [CrossRef]
15. Guan, X.; Wu, H.; Shi, Y.; Dai, D. Extremely small polarization beam splitter based on a multimode interference coupler with a silicon hybrid plasmonic waveguide. *Opt. Lett.* **2014**, *39*, 259–262. [CrossRef]
16. Xu, L.; Wang, Y.; Kumar, A.; Patel, D.; El-Fiky, E.; Xing, Z.; Li, R.; Plant, D.V. Polarization beam splitter based on MMI coupler with SWG birefringence engineering on SOI. *IEEE Photonics Technol. Lett.* **2018**, *30*, 403–406. [CrossRef]
17. Xu, L.; Wang, Y.; El-Fiky, E.; Mao, D.; Kumar, A.; Xing, Z.; Saber, M.G.; Jacques, M.; Plant, D.V. Compact broadband polarization beam splitter based on multimode interference coupler with internal photonic crystal for the SOI platform. *J. Lightwave Technol.* **2019**, *37*, 1231–1240. [CrossRef]
18. Lin, Z.; Chen, K.; Huang, Q.; He, S. Ultra-Broadband Polarization Beam Splitter Based on Cascaded Mach-Zehnder Interferometers Assisted by Effectively Anisotropic Structures. *IEEE Photonics J.* **2021**, *13*, 1–9. [CrossRef]
19. Zou, J.; Yu, Y.; Zhang, X. Two-dimensional grating coupler with a low polarization dependent loss of 0.25 dB covering the C-band. *Opt. Lett.* **2016**, *41*, 4206–4209. [CrossRef]
20. Zhang, Z.; Chen, X.; Cheng, Q.; Khokhar, A.Z.; Zhang, Z.; Yan, X.; Huang, B.; Chen, H.; Liu, H.; Li, H.; et al. Two-dimensional apodized grating coupler for polarization-independent and surface-normal optical coupling. *J. Lightwave Technol.* **2020**, *38*, 4037–4044. [CrossRef]
21. Zou, J.; Yu, Y.; Zhang, X. Single step etched two dimensional grating coupler based on the SOI platform. *Opt. Express* **2015**, *23*, 32490–32495. [CrossRef] [PubMed]
22. Dai, D.; Bowers, J.E. Novel ultra-short and ultra-broadband polarization beam splitter based on a bent directional coupler. *Opt. Express* **2011**, *19*, 18614–18620. [CrossRef] [PubMed]
23. Wang, X.; Quan, X.; Zhang, W.; Hu, J.; Shen, C.; Cheng, X. Ultra-small and fabrication-tolerant silicon polarization beam splitter using sharp bent directional coupler. *IEEE Photonics J.* **2018**, *10*, 1–7. [CrossRef]
24. Fu, P.H.; Huang, T.Y.; Fan, K.W.; Huang, D.W. Optimization for ultrabroadband polarization beam splitters using a genetic algorithm. *IEEE Photonics J.* **2018**, *11*, 1–11. [CrossRef]
25. Shen, B.; Wang, P.; Polson, R.; Menon, R. An integrated-nanophotonics polarization beamsplitter with 2.4 × 2.4 μm^2 footprint. *Nat. Photonics* **2015**, *9*, 378–382. [CrossRef]

26. Liu, X.; Liu, D.; Dai, D. Silicon polarization beam splitter at the 2 µm wavelength band by using a bent directional coupler 166 assisted with a nano-slot waveguide. *Opt. Express* **2021**, *29*, 2720–2726. [CrossRef]
27. Lalau-Keraly, C.M.; Bhargava, S.; Miller, O.D.; Yablonovitch, E. Adjoint shape optimization applied to electromagnetic design. *Opt. Express* **2013**, *21*, 21693–21701. [CrossRef]
28. GitHub. Scipy/Scipy/ at v1.8.0. Available online: https://github.com/scipy/scipy/tree/v1.8.0 (accessed on 18 April 2022).
29. Zhou, M.; Lazarov, B.S.; Wang, F.; Sigmund, O. Minimum length scale in topology optimization by geometric constraints. *Comp. Methods Appl. Mech. Eng.* **2015**, *293*, 266–282. [CrossRef]
30. Zhang, G.; Liboiron-Ladouceur, O. Scalable and low crosstalk silicon mode exchanger for mode division multiplexing system enabled by inverse design. *IEEE Photonics J.* **2021**, *13*, 1–13. [CrossRef]
31. Wen, X.; Xu, K.; Song, Q. Design of a barcode-like waveguide nanostructure for efficient chip–fiber coupling. *Photonics Res.* **2016**, *4*, 209–221. [CrossRef]
32. Xu, K.; Liu, L.; Wen, X.; Sun, W.; Zhang, N.; Yi, N.; Sun, S.; Xiao, S.; Song, Q. Integrated photonic power divider with arbitrary power ratios. *Opt. Lett.* **2017**, *42*, 855–858. [CrossRef] [PubMed]
33. Taflove, A. Application of the finite-difference time-domain method to sinusoidal steady-state electromagnetic-penetration problems. *IEEE Trans. Electromagn. Compat.* **1980**, *3*, 191–202. [CrossRef]
34. Lu, L.; Liu, D.; Zhou, F.; Li, D.; Cheng, M.; Deng, L.; Fu, S.; Xia, J.; Zhang, M. Inverse-designed single-step-etched colorless 3 dB couplers based on RIE-lag-insensitive PhC-like subwavelength structures. *Opt. Lett.* **2016**, *41*, 5051–5054. [CrossRef] [PubMed]
35. Augenstein, Y.; Rockstuhl, C. Inverse design of nanophotonic devices with structural integrity. *ACS Photonics* **2020**, *7*, 2190–2196. [CrossRef]
36. Su, L.; Piggott, A.Y.; Sapra, N.V.; Petykiewicz, J.; Vuckovic, J. Inverse design and demonstration of a compact on-chip narrowband three-channel wavelength demultiplexer. *ACS Photonics* **2018**, *5*, 301–305. [CrossRef]
37. Piggott, A.Y.; Ma, E.Y.; Su, L.; Ahn, G.H.; Sapra, N.V.; Vercruysse, D.; Netherton, A.M.; Khope, A.S.; Bowers, J.E.; Vuckovic, J. Inverse-designed photonics for semiconductor foundries. *ACS Photonics* **2020**, *7*, 569–575. [CrossRef]
38. Xu, H.; Dai, D.; Shi, Y. Ultra-broadband and ultra-compact on-chip silicon polarization beam splitter by using hetero-anisotropic metamaterials. *Laser Photonics Rev.* **2019**, *13*, 1800349. [CrossRef]
39. Herrero-Bermello, A.; Dias-Ponte, A.; Luque-González, J.M.; Ortega-Moñux, A.; Velasco, A.V.; Cheben, P.; Halir, R. Experimental demonstration of metamaterial anisotropy engineering for broadband on-chip polarization beam splitting. *Opt. Express* **2020**, *28*, 16385–16393. [CrossRef]
40. Li, C.; Zhang, M.; Bowers, J.E.; Dai, D. Ultra-broadband polarization beam splitter with silicon subwavelength-grating waveguides. *Opt. Lett.* **2020**, *45*, 2259–2262. [CrossRef]